Inferring the seasonal evolution of phytoplankton groups in the Senegalo-Mauritanian upwelling region from satellite ocean-color spectral measurements

Ousmane Farikou, Salam Sawadogo, Awa Niang, Daouda Diouf, Julien Brajard, Carlos Mejia, Yves Dandonneau, G. Gasc, Michel Crépon, Sylvie Thiria

AGU PUBLICATIONS

JGR

Journal of Geophysical Research: Oceans

RESEARCH ARTICLE

10.1002/2015JC010738

Key Points:
- We processed SeaWiFS observations covering 13 years
- We estimated phytoplankton groups in the Senegalo-Mauritanian upwelling region
- Diatoms are dominant when the upwelling intensity is maximal (April–May)

Correspondence to:
M. Crepon,
crepon@locean-ipsl.upmc.fr

Citation:
Farikou, O., S. Sawadogo, A. Niang, D. Diouf, J. Brajard, C. Mejia, Y. Dandonneau, G. Gasc, M. Crepon, and S. Thiria (2015), Inferring the seasonal evolution of phytoplankton groups in the Senegalo-Mauritanian upwelling region from satellite ocean-color spectral measurements, *J. Geophys. Res. Oceans*, *120*, 6581–6601, doi:10.1002/2015JC010738.

Received 21 JAN 2015
Accepted 9 SEP 2015
Accepted article online 14 SEP 2015
Published online 30 SEP 2015

Inferring the seasonal evolution of phytoplankton groups in the Senegalo-Mauritanian upwelling region from satellite ocean-color spectral measurements

O. Farikou[1,2], S. Sawadogo[3], A. Niang[1], D. Diouf[1], J. Brajard[4], C. Mejia[4], Y. Dandonneau[4], G. Gasc[4], M. Crepon[4], and S. Thiria[4,5]

[1]Ecole Supérieure Polytechnique, Université Cheikh Anta Diop, Dakar, Senegal, [2]Institut Universitaire des Sciences et Techniques d'Abéché, Abéché, Chad, [3]Ecole Polytechnique de Thiès, Thiès, Senegal, [4]IPSL/LOCEAN, Sorbonne Université, Université Paris 6, CNRS-IRD-UPMC-MNHN, Paris, France, [5]UVSQ, F-78035, Versailles, France

Abstract We have investigated the phytoplankton dynamics of the Senegalo-Mauritanian upwelling region, which is a very productive region, by processing a 13 year set of SeaWiFS satellite ocean-color measurements using a PHYSAT-like method. We clustered the spectra of the ocean-color normalized reflectance (reflectance normalized by a reflectance dependent on chlorophyll-*a* concentration only) into 10 significant spectral classes using a Self-Organized Map (SOM) associated with a hierarchical ascendant classification (HAC). By analyzing a 13 year climatology of these classes, we have been able to outline a coherent scenario describing the Senegalo-Mauritanian upwelling region in terms of spatiotemporal variability of phytoplankton groups: during the onset of the upwelling (December–February), we mainly observed nanoeukaryote-type phytoplankton in the coastal area; in April–May, the period corresponding to the maximum chlorophyll-*a* concentration, the nanoeukaryote types were replaced by diatom types. This scenario is in agreement with microscope phytoplankton cell observations done during several past cruises.

1. Introduction

The Senegalo-Mauritanian upwelling off the west coast of Africa is the southern part of the Canary upwelling system. It is a very active oceanic region in biological terms with strong economic impacts on fisheries in Senegal and Mauritania. We focused our study on the region south of 20°N between 8°N and 24°N and 14°W and 30°W (Figure 1) where the upwelling presents a well-marked seasonal variability driven by the intensity of the wind component parallel to the coast. This region has been intensively studied by analysis of SeaWiFS ocean-color data and AVHRR sea surface temperature as reported in *Demarcq* and *Faure* [2000] and more recently by *Sawadogo et al.* [2009] and *Farikou et al.* [2013]. These authors have noted the presence of an intense upwelling, both in the ocean-color signal and in the sea surface temperature (SST). They observed very high chlorophyll-*a* concentration near the shore and a rapidly decreasing concentration offshore. The upwelling intensity is maximum in March–April and weakens in July–August with the arrival of the intertropical convergence zone (ITCZ) from the south and the decrease in the intensity of the trade winds [*Farikou et al.*, 2013]. Since this region has been poorly surveyed in situ, we have chosen to extract pertinent biological information from ocean-color satellite multispectral measurements. Satellite sensors provide a tremendous amount of data which remain unexploited due to the lack of adequate methods for processing large data sets. This satellite information should help to improve understanding of the functioning of a poorly surveyed region such as the Sénégalo-Mauritanian upwelling region, to detect the points of interest on which specific research efforts should be focused, and ultimately to contribute to the improved design of oceanographic cruises and the optimization of the research vessel tracks for in situ sampling purposes.

Ocean-color measurements have been intensively used to investigate chlorophyll-*a* concentration (Chl-*a*; mg m^{-3}) in the surface waters of the ocean [*O'Reilly et al.*, 1998]. The main objective was first to compute phytoplankton primary production [*Longhurst et al.*, 1995; *Antoine et al.*, 1996; *Behrenfeld and Falkowski*, 1997; *Behrenfeld et al.*, 2006; *Westberry et al.*, 2008]. Recently, it has been shown that it is also possible to extract additional information such as phytoplankton size classes (PSC) [*Uitz et al.*, 2006; *Ciotti and Bricaud*, 2006; *Hirata et al.*, 2008; *Mouw and Yoder*, 2010] and even phytoplankton groups [*Sathyendranath et al.*, 2004;

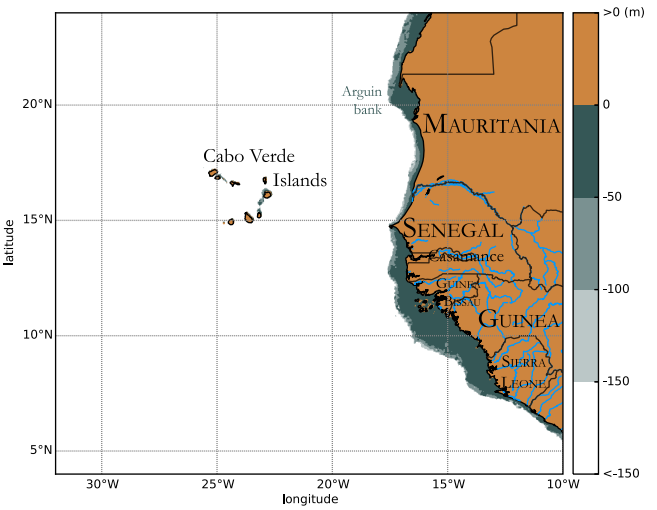

Figure 1. Mauritania and Senegal coastal topography. The land is in *brown* and the ocean depth is represented by the color scale in meters (right-hand side of the figure).

Alvain et al., 2005, 2012; *Hirata et al.*, 2011], which is of fundamental interest to understand the phytoplankton behavior and to model its evolution. Phytoplankton is the first element in ocean food webs and consequently drives the ocean productivity. It also plays a fundamental role in climate regulation by trapping atmospheric CO_2 through gaseous exchange at the sea surface. With the growing interest in a changing climate, one may ask how the different phytoplankton populations will respond to changes in ocean characteristics (temperature, salinity) and nutrient supply, and what will be their impact on the climate.

We propose to determine the seasonal variability of some phytoplankton groups in the Sénégalo-Mauritanian region by using a PHYSAT regional procedure. The PHYSAT method [*Alvain et al.*, 2005] is based on the analysis of ocean-color spectra. The phytoplankton species present different spectral signatures due to the absorption properties of their specific pigments and the backscattering of incoming solar radiation due to the composition and the shape of their cell wall. By analyzing in situ measurements of phytoplankton pigments in terms of SeaWiFS water-leaving spectral reflectances normalized to a reflectance depending on chlorophyll-*a* concentration only, these authors clustered the SeaWiFS normalized spectral reflectances into four classes, each of them being related to a predominant phytoplankton group. The normalization procedure, which is a key ingredient of the method, aims at focusing the analysis on the spectrum shape, independently of the chlorophyll-*a* concentration, and should allow the detection of phytoplankton groups from space observations. The PHYSAT method was first developed on collocation between 41 in situ measurements and SeaWiFS observations at global scale (GeP&CO data base) [*Alvain et al.*, 2005]. The clustering was done by a visual inspection of the shape of the spectrum. A rationalization of the method was presented in *Ben Mustapha et al.* [2014], who used a one-step neural network clustering, which permitted an efficient partition based on objective criteria of an extended database constituted by 1068 coincident in situ and satellite ocean-color measurements and consequently to obtain an improved spectrum labeling.

Since we do not have concomitant in situ measurements in the studied region, our strategy is based on group identification, such as those determined by *Ben Mustapha et al.* [2014] at global scale, on the one hand, and on the coherence of the patterns of the different phytoplankton groups both in space and in time with respect to the upwelling dynamics in that region, on the other hand.

In the present paper, we analyze the ocean-color spectrum provided by the SeaWiFS daily observations with a special focus on the identification of phytoplankton groups and their seasonal variability in the studied region. Section 2 describes the ocean-color data we processed. Section 3 presents the classification methodology we used. Since we analyzed a very large amount of data (13 years of SeaWiFS daily observations), we used an efficient two-step clustering method to evidence the most significant spectra. Section 4 is devoted to the analysis of the ocean-color spectra. Section 5 analyses the results in the region studied. In section 6, we attempt to attribute phytoplankton groups to the spectral classes and to describe an upwelling scenario for these phytoplankton groups as revealed by our SeaWiFS analysis. Section 7 is devoted to a discussion and a conclusion.

2. The Data

We used the daily water-leaving reflectances, $\rho_W(\lambda)$, at a 4 km resolution, computed by *Diouf et al.* [2013], which are available at: http://poacc.locean-ipsl.upmc.fr/. These water-leaving reflectances were obtained by

processing the SeaWiFS daily reflectances, $\rho^{obs}{}_{TOA}w(\lambda)$, provided by the NASA/GSFC/DAAC observed at the top of the atmosphere (TOA) with the SOM-NV (SOM-NeuroVaria) algorithm [*Diouf et al*., 2013] from 1998 to 2010. This algorithm was specifically trained to take desertic dusts into account in the atmospheric correction process. The desertic dusts which are abundant in the studied region, absorb the sun light, and influence the TOA spectra and consequently may perturb the measurements of ocean reflectance spectra, which depend on the absorption properties of the phytoplankton-specific pigments. It is therefore important to efficiently compute the effect of desertic dusts in the atmospheric correction process in order to obtain ocean reflectrance spectra which depend on phytoplankton only. In the present study, we used water-leaving reflectances at five wavelengths (412, 443, 490, 510, and 555 nm). In order to extract the second-order effect due to specific water characteristics other than phytoplankton abundance, we computed a reflectance ratio, $Ra(\lambda)$, defined following *Alvain et al*. [2012] as:

$$Ra(\lambda)=\rho_W(\lambda)/\rho_W^{ref}(\lambda,\ \text{Chl-}a) \tag{1}$$

where $\rho_W^{ref}(\lambda,$ Chl-$a)$ is a simple model of $\rho_W(\lambda)$ that only accounts for the SeaWiFS standard chlorophyll-*a* concentration provided by the NASA.

The computation of $Ra(\lambda)$ (see equation (1)) implies the knowledge of $\rho_W^{ref}(\lambda,$ Chl-$a)$. Such a model has been estimated by *Alvain et al*. [2005] by collocating in situ observations of chlorophyll-*a* and high-quality SeaWiFs $\rho_W(\lambda)$ measurements. But this model is only valid for chlorophyll-*a* concentrations in the range 0.03–3 mg m^{-3}, whereas we have to deal with chlorophyll-*a* concentrations reaching values greater than 10 mg m^{-3} in the studied region. We therefore decided to compute a new $\rho_W^{ref}(\lambda,$ Chl-$a)$ model valid for chlorophyll-*a* concentrations up to 10 mg m^{-3}. These very high chlorophyll-*a* concentrations may be spoilt by errors as they are outside the limit of validity of the OC4V4 algorithm used in the SOM-NV method; the corresponding data will be used with care. Moreover, as the *Alvain et al*. [2005] model is given in the form of a discrete array (LUT), which implies interpolation of the actual chlorophyll-*a* concentration values between two discrete chlorophyll-*a* values, we chose to build a new $\rho_W^{ref}(\lambda,$ Chl-$a)$ model as a continuous function of SeaWiFS chlorophyll-*a* concentration values by using a specific class of neural networks, the so-called MLP (Multi-Layer Perceptron), which are well-suited estimators for nonlinear continuous regression [*Bishop*, 2006; *Thiria et al*., 1993]. As the function Chl-$a \rightarrow \rho_W^{ref}(\lambda,$ Chl-$a)$ is very different for each λ, we computed an MLP for each of the five visible SeaWiFS λ values (412, 443, 490, 515, and 555 nm). This model was calibrated on 127 daily SeaWiFS images in the studied region from the year 2003. In order to reduce the number of vectors, which was enormous, we only sampled one pixel-line over 10 of the daily SeaWiFS images from the year 2003. We then computed the $Ra(\lambda)$ from the SeaWiFS daily values from 1998 to 2010.

We now propose to cluster the $Ra(\lambda)$ spectra into different classes to try to evidence different phytoplankton groups.

3. The Classification Methodology

The classification methodology is similar to that used by *Farikou et al*. [2013] in the study of the Senegalo-Mauritanian upwelling and by *Lachkar and Gruber* [2012] for the eastern boundary upwelling regions. First we used a specific classification model based on a neural network, the so-called Self-Organizing Map (SOM in the following), which was first introduced by *Kohonen* [1982]. The SOM is an unsupervised classification method made of a competitive neural network structured in two layers (Figure 2). The first layer (or input layer) receives the vector data *R* (the five $Ra(\lambda)$ values). Each neuron *j* of the second layer (Figure 2) is associated with a particular reference vector (*Rv*) representing a typical $Ra(\lambda)$ spectrum and thus corresponds to a cluster (a set of $Ra(\lambda)$ spectra) [*Jouini et al*., 2013, *Niang et al*., 2003, 2006]. The referent vectors *Rvs* are determined from a learning data set $\boldsymbol{L}$ statistically representative of the analyzed data set through an iterative learning process. The referent vectors are first initialized to evenly distributed values of the $Ra(\lambda)$ values in the range of the learning set and then computed by minimizing a nonlinear cost function as in the *k*-means algorithm [*Badran et al*., 2005]. Then, for each R_i of the learning set presented to the SOM, the Euclidian distance between R_i and the referent vectors *Rvs* are computed and the closest referent vector Rv_j is selected. The referent vectors *Rvs* of the SOM are then updated and their topological neighbors are changed in order to better match the input vector. Each neuron *j* is associated with a subset $\boldsymbol{J}$ (or a cluster) of $\boldsymbol{L}$ that gathers

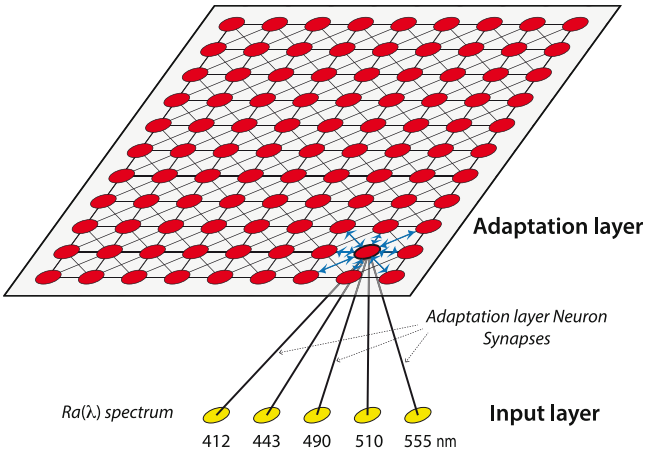

Figure 2. Structure of the self-organizing map (SOM). The network comprises two layers: an input layer used to present observations ($Ra(\lambda)$ spectrum) and an adaptation layer (whose neurons are represented in *red*), which is an active layer for which a neuron neighborhood system is defined (schematized by the *blue arrows*). Each neuron *i* is fully connected to the input layer by its synapses whose weights are set to the input layer values. Each neuron of the adaptation layer is associated with a reference vector, rv_i representing a set of $Ra(\lambda)$ spectra having close similarities and computed following *Kohonen* [2001].

data, which are close together according to the cost function and have common characteristics. The referent vector Rv_j synthesizes the data characteristics of the subset $\boldsymbol{J}$.

In the present study, we deal with a two-dimensional SOM map with quite a large number of neurons (20 × 20) and thus of *Rvs*, providing a highly discriminating representation of the observations. The $Ra(\lambda)$ of the analyzed data set is thus partitioned into 400 clusters. We used the SOM version available on the web site http://www.cis.hut.fi/projects/somtoolbox/download/. The topological map was trained according to the procedure described in *Kohonen* [2001]. The number of neurons was determined empirically from solutions of similar problems and then adjusted as described by *Badran et al.* [2005]. The learning data set $\boldsymbol{L}$ is composed of the $Ra(\lambda)$ daily values for the year 2003, a year in which the cloud coverage was the lowest with respect to the 13 years of observations.

The large number of clusters allowed us to take into account the complexity of the data set but may have prevented us from synthesizing some geophysical information embedded in the data, such as spatial or seasonal specificities. To counteract this difficulty, we decided to aggregate this large number of clusters into a smaller number of classes based on the similarities of the clusters. We thus extracted a few pertinent classes from the clusters by merging clusters with similar statistical properties, expecting the classes to be associated with similar geophysical characteristics. For this, we used a hierarchical ascendant classification (HAC in the following), which is a bottom-up hierarchical classification [*Jain and Dubes*, 1998]. This method iteratively computes a partition hierarchy of the clusters. From the initial partition (the neurons or clusters on the map), two subsets of the computed partition are gathered at each iteration. These two subsets are selected by measuring their similarity according to the Ward criterion.

We aggregated the 20 × 20 neurons into 10 significant classes. The resulting clustering of the five dimension vectors, *Rvs*, associated with the neurons of the topological map is given in Figure 3. The map represents a topological space associated with the neurons: the closer the neurons on the map, the more similar the *Rvs*. We note that the topological map + HAC clustering is very coherent, since the classes represent clusters whose neurons are contiguous on the topological map. Moreover, the spectra associated with each neuron (or *Rv*) determine homogeneous fields on the SOM. The number of classes (10) was selected because it presented the most significant discriminative partition with respect to the full dendrogram of the HAC (Figure 4), on the one hand, and to the spectrum homogeneity (Figure 5), on the other hand. Ten classes correspond to statistically well-defined entities whose patterns are well marked. Moreover during the exploratory phase of that exercise, it is wise to use a quite high number of classes. At the end of our research, it shall be possible to merge some classes according to their statistical (dendogram structure) and geographical attributes as discussed in section 7.

This two-step clustering method (SOM+HAC) is different from this of *Ben Mustapha et al.* [2014] who used a one-step method (SOM) which does not allow some analysis linking the different classes permitted by our method (see section 7).

4. $Ra(\lambda)$ Spectrum Significance

The spectra of the different classes are well defined, each spectrum presenting a well-marked shape not overlapping any others (Figure 5). The different class spectra (spectrum associated with each neuron of a

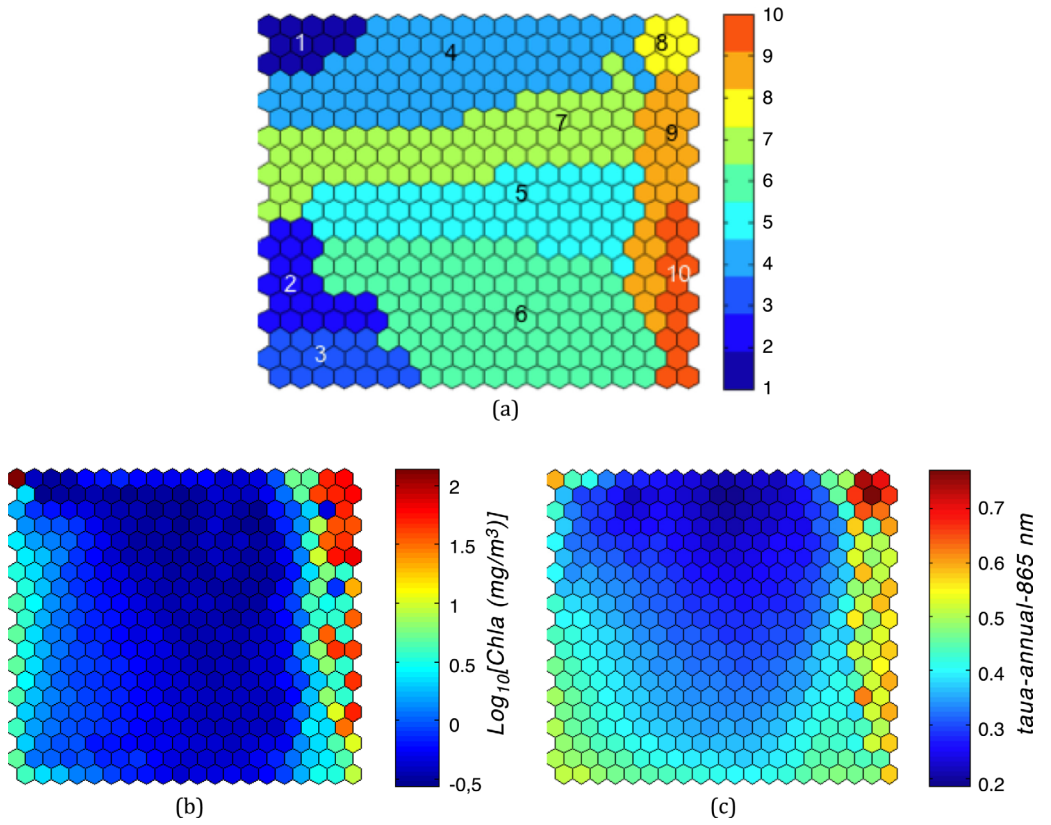

Figure 3. (a) Representation of the 10 classes on the SOM map. Each class is represented by a different color. (b) Chlorophyll-*a* concentration associated with each reflectance anomaly captured by each neuron. (c) Mean optical depth associated with each reflectance anomaly captured by each neuron of the SOM. The color bar on the right is the AOT value scale.

class) are close together, the intraclass variance being small (except at 412 nm for class-4, class-5, and class-7). This shows that the SOM clustering has functioned well and that the different spectra are probably associated with well-marked phenomena.

Class-8, class-9, and class-10, which are close together on the SOM map (Figure 3a), are associated with very high chlorophyll-*a* (Figure 3b) and with three dendogram branches (Figure 4) connected to the same node. They are characterized by a low-spectrum value at 412 nm (Figure 5). This low 412 nm value is due to a number of factors that include the presence of absorption of blue photons by colored dissolved organic matter of various origins, by phytoplankton pigments and also by possible inaccuracies in atmospheric correction in this wavelength region (see below). As an example, if atmospheric correction is subtracting off too much blue radiance, this may depress the blue end of the spectrum. The high values of the class-10 spectrum at wavelengths of 510 and 555 nm correspond to backscattering due to suspended particles. The pixels of these three classes are located

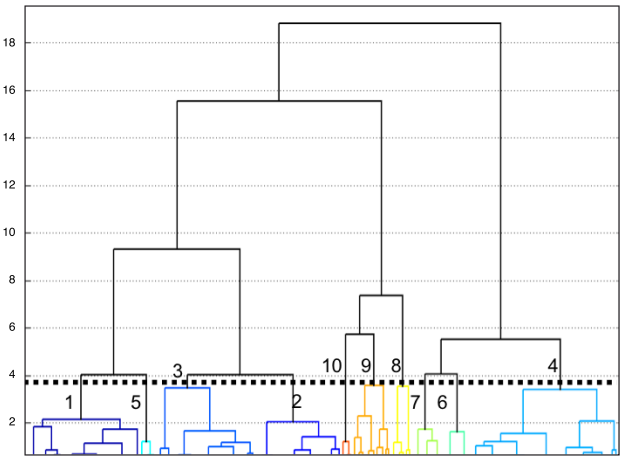

Figure 4. Dendogram of the HAC.

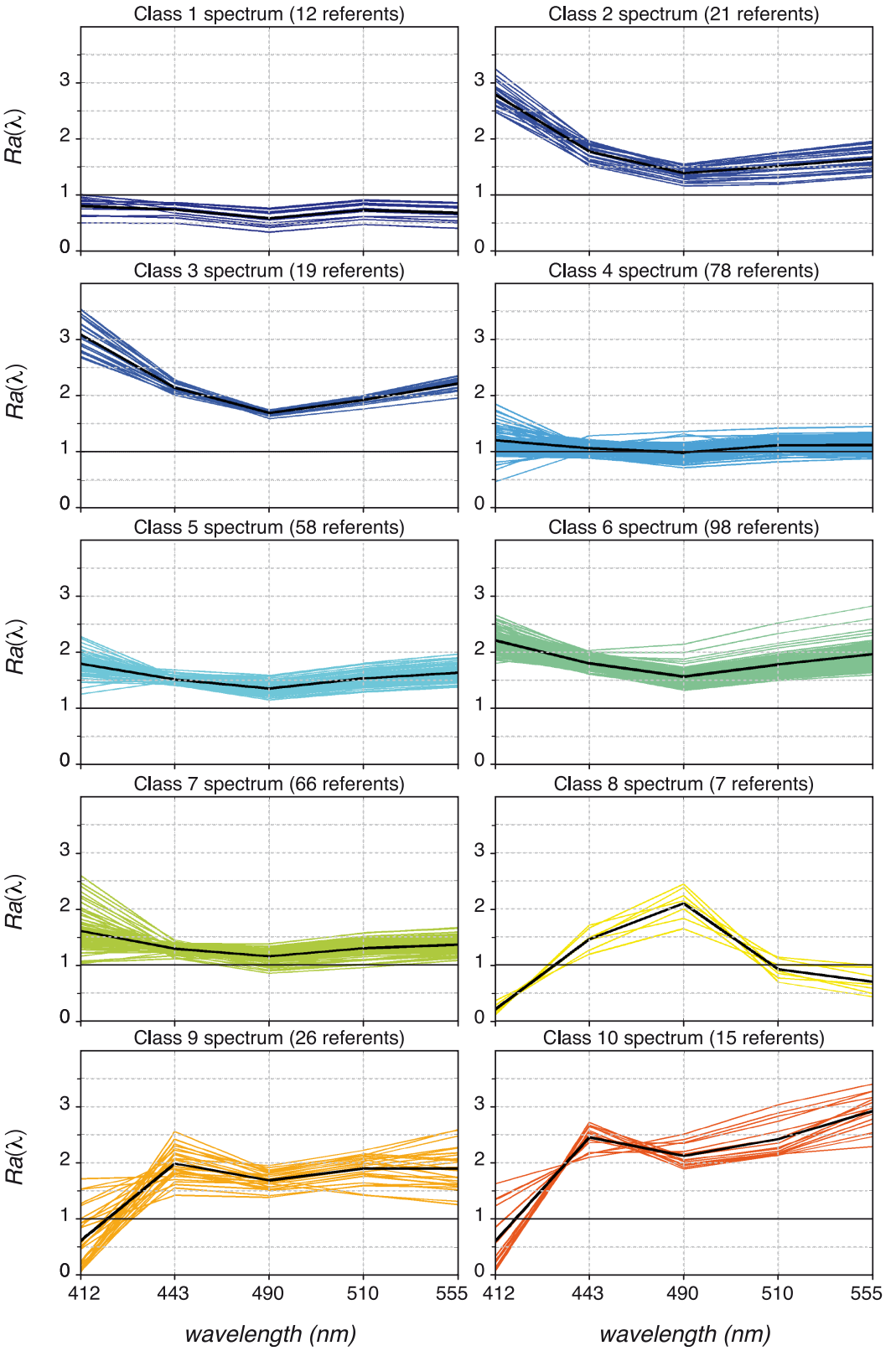

Figure 5. Representation of the 10 reflectance ratio spectra. The *solid black line* represents the mean ratio spectrum of each class.

in geographical regions corresponding to coastal waters, such as the Arguin Bank (20°N) and the continental shelf off the Siné-Saloum, Casamance, and Guinea coasts (8°N–13°N) (Figure 1), which are very shallow regions, presenting dissolved terrigenous material responsible for high absorption at 412 nm and suspended particles due to bottom erosion and responsible for backscattering light (class-10 spectrum). Due to the very coastal location of their pixels and their spectral shape, class-8, class-9, and class-10 correspond to case-2 waters [*Morel*, 1980; *Prieur and Sathyendranath*, 1981]. In such waters, the PHYSAT method for identifying phytoplankton groups cannot apply, since we used the calibration of PHYSAT given by *Ben Mustapha et al*, [2014], which was developed for case-1 waters only. This is why we decided to focus our analysis only on class-1 to class-7, whose spectra correspond to case-1 waters [*Ben Mustapha et al*, 2014], and which are located in areas whose depth is deeper than areas corresponding to class-8, class-9, and class-10. Moreover class-1 to class-7 are associated with low AOT values (less than 0.35 in the average, Figure 3c), which minimize the influence of atmosphere on the spectra characteristics. We also removed observations of neuron 1 of class-1 whose data are highly contaminated by the atmosphere, as shown by the high value of its mean AOT (Figure 3c).

Class analysis is very sensitive to spectra that may have been contaminated by small defects in the atmospheric correction. In order to check that point, we have represented the mean atmospheric optical thickness (AOT in the following) that is associated with the reflectances captured by each neuron (Figure 3c) of the SOM. In that figure, we see that class-1, class-4, class-5, class-6, and class-7 are associated with low AOT values, class-2 and class-3 with quite moderate AOT values. We found that the shapes of the spectra were not distorted due to inaccurate atmospheric correction, and truly represented the optical properties of the water. In order to confirm this, we averaged the spectra captured by each neuron of a class for which AOT < 0.35 and compared them to the mean spectrum of that class whatever its AOT, for class-1 to class-7. Comparison between the mean spectrum for which AOT < 0.35 and the spectrum assigned to a class shows that the two categories of spectrum are close together (Figure 6). This is partly due to the computation of the ocean reflectance, $\rho_W(\lambda)$, with the SOM-NV method which is specially designed to take into account absorbing aerosols such Saharan dusts. This supports the ability of a spectrum to retrieve ocean parameters independently of the AOT value of the analyzed pixel. We note that the form of the class-2 spectrum is somewhat affected by the procedure, showing a well-marked peak at 510 nm for a spectrum corresponding to observations whose AOT is less than 0.35, which is characteristic of diatoms [*Alvain et al*., 2012].

5. Seasonal Evolution of the Different Classes

In order to study the seasonal variability of the different $Ra(\lambda)$ classes with some statistical confidence, we constructed a monthly climatology of the classes for 13 years (1998–2010) of the SeaWiFS observations. Each pixel of the geographical map was associated with 10 counters corresponding to the ten classes. The counters were set to zero at the beginning of each month of 1998. The first day of the month was projected onto the SOM; the counter of the class associated with each pixel was incremented by unity. Then the second day was projected onto the SOM; the counter of the class associated with each pixel was incremented by unity. This iteration was continued until the last day of each month of 2010. At the end of each month, the pixel class was the class of the winning counter. The resulting climatology is presented for November and December in Figure 7a, for January, February, and March in Figure 7b, and for April, May, and June in Figure 7c. To better visualize the class variability, we show the monthly evolution of the seven classes in two figures, one for class-1, class-4, and class-6 (Figures 7a–7c, left) and the other for class-2, class-3, class-5, and class-7 (Figures 7a–7c, right). Most of the time, the class pixel is determined without ambiguity: i.e., the winning counter having a much higher score than the others. We note that the classes are represented by contiguous pixels on the geographical maps, defining well-structured patterns. Moreover, the classes present a well-marked seasonality. In the center of a geographical patch of a class, the class is very dominant; its relative frequency of occurrence is higher than 90%, as found on the class histogram (not shown).

Class-1 (Figure 7a, left) starts developing in November in the northern part of the Mauritanian upwelling region where the chlorophyll extends far offshore, transported by eddies and filaments [*Lathuilière et al*., 2008]. In the Senegal region (12°N–16°N), class-1 is well marked in the coastal area in January and February

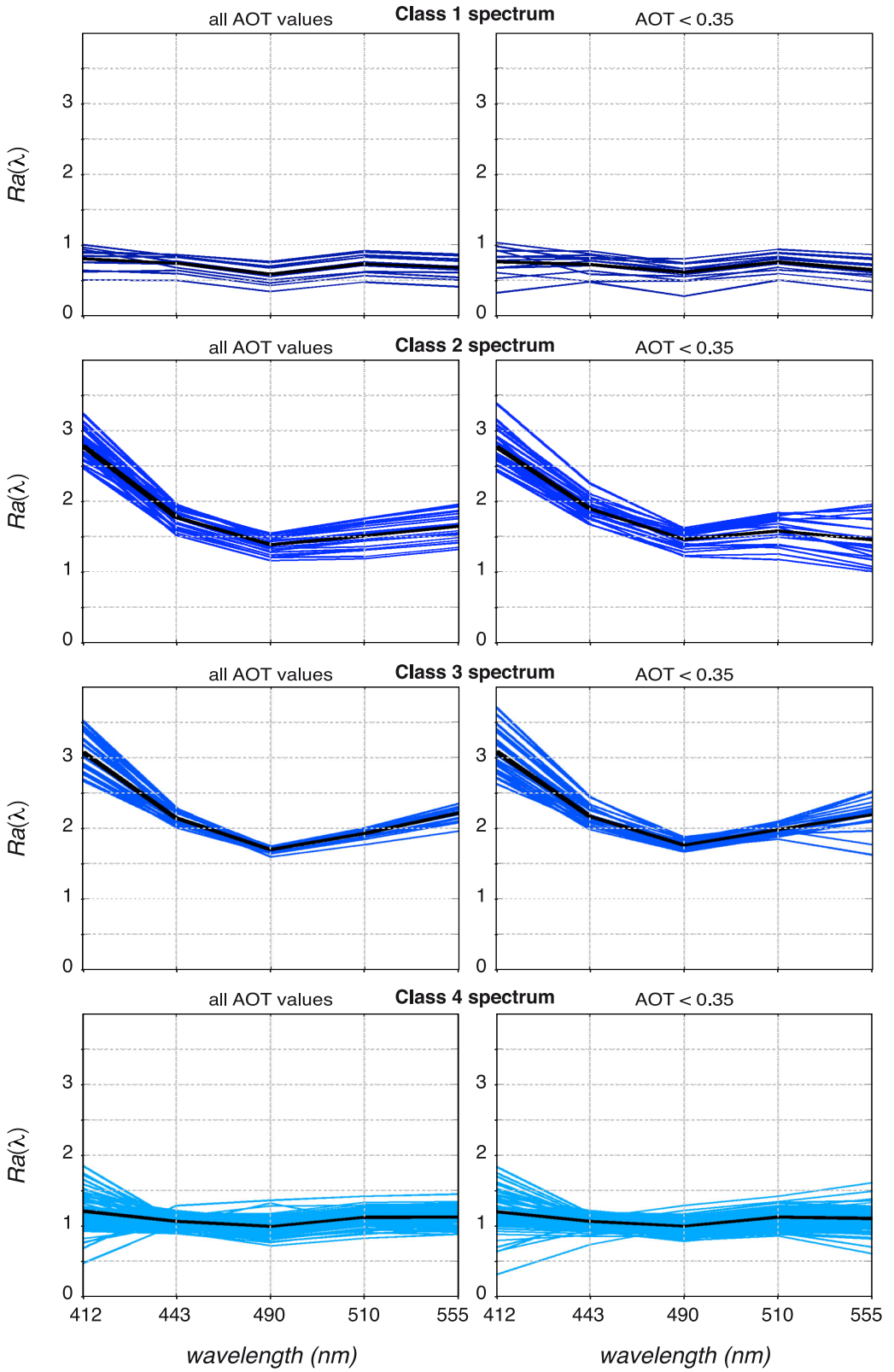

Figure 6. Comparison between the reflectance (left) ratio spectra 1, 2, 3, and 4 given by SOM whatever the AOT value is, and (right) ratio spectra given by SOM for observations for which AOT < 0.35. The two ratio spectra are very similar showing that AOT does not affect the ratio spectrum shape too much. Note the small peak at 512 nm for class-2 spectrum, which is typical of diatom spectra.

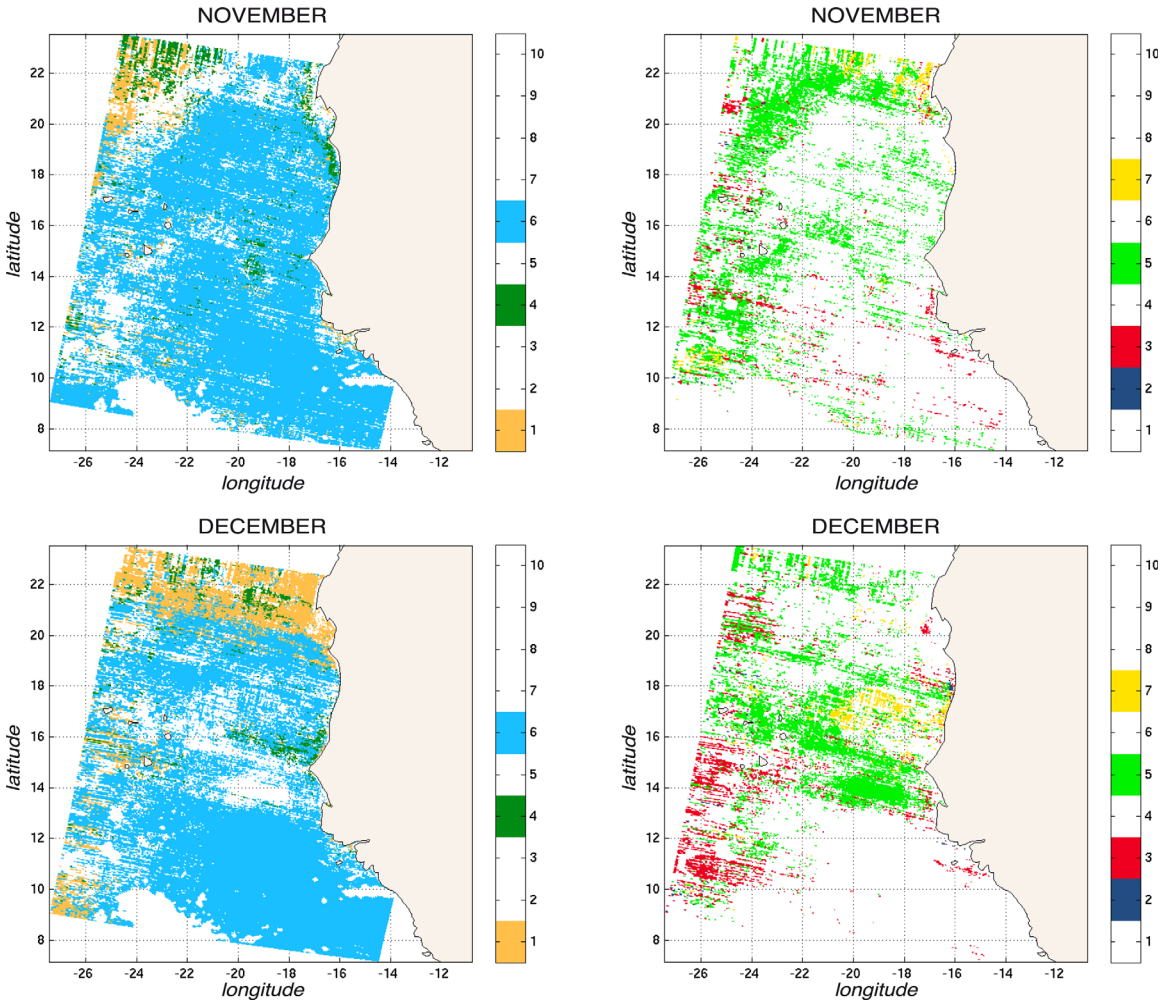

Figure 7a. The 13 year climatology of the classes for November and December. (left) We have represented class-1 (*orange*), class-4 (*green*), and class-6 (*light blue*). (right) We have represented class-2 (*blue*), class-3 (*red*), class-5 (*light green*), and class-7 (*yellow*).

(Figure 7b, left) and disappears in March (Figure 7b, left) until November. Class-4 is associated with offshore waters bounding the western part of class-1 waters and can occupy the coastal area in February, replacing class-1 waters in some places (Figure 7b, left). It is still encountered in the northern part of the studied region in April, May, and June far offshore (Figure 7c, left) and then disappears until January.

Class-3 (Figure 7b, right) is encountered in offshore regions in March mainly north of 14°N. It is well developed in the coastal area in April (Figure 7c, right) when the upwelling intensity is maximum (Figure 8), replacing class-1 waters. Class-3 waters are associated with some patches of class-2 waters. In May, there is a narrow strip of class-2 and class-3 waters which follows the coastal upwelling in the southern part of the studied region between 10°N and 14°N, while well-developed patches of class-3 waters are encountered offshore North of 14°N. These class-2 and class-3 patterns are still present offshore in June (Figure 7c, right). A well-defined patch of class-7 water is visible in May between 16°N and 20°N replacing the class-3 water (Figure 7c, right). The signature of this patch is still visible in June. Class-2, class-3, and class-7 disappear until the following March.

Class-6 water (Figures 7a–7c, left) is present in all seasons. It is found in the south part of the studied region in January–February and, starting in March, it moves northward and occupies the whole region in April.

Class-5 is situated between class-7 and class-6 in the SOM (Figure 3a); its $Ra(\lambda)$ spectrum shape is similar to that of the latter two classes, but it is associated with a dendogram branch far away from these two classes (Figure 4).

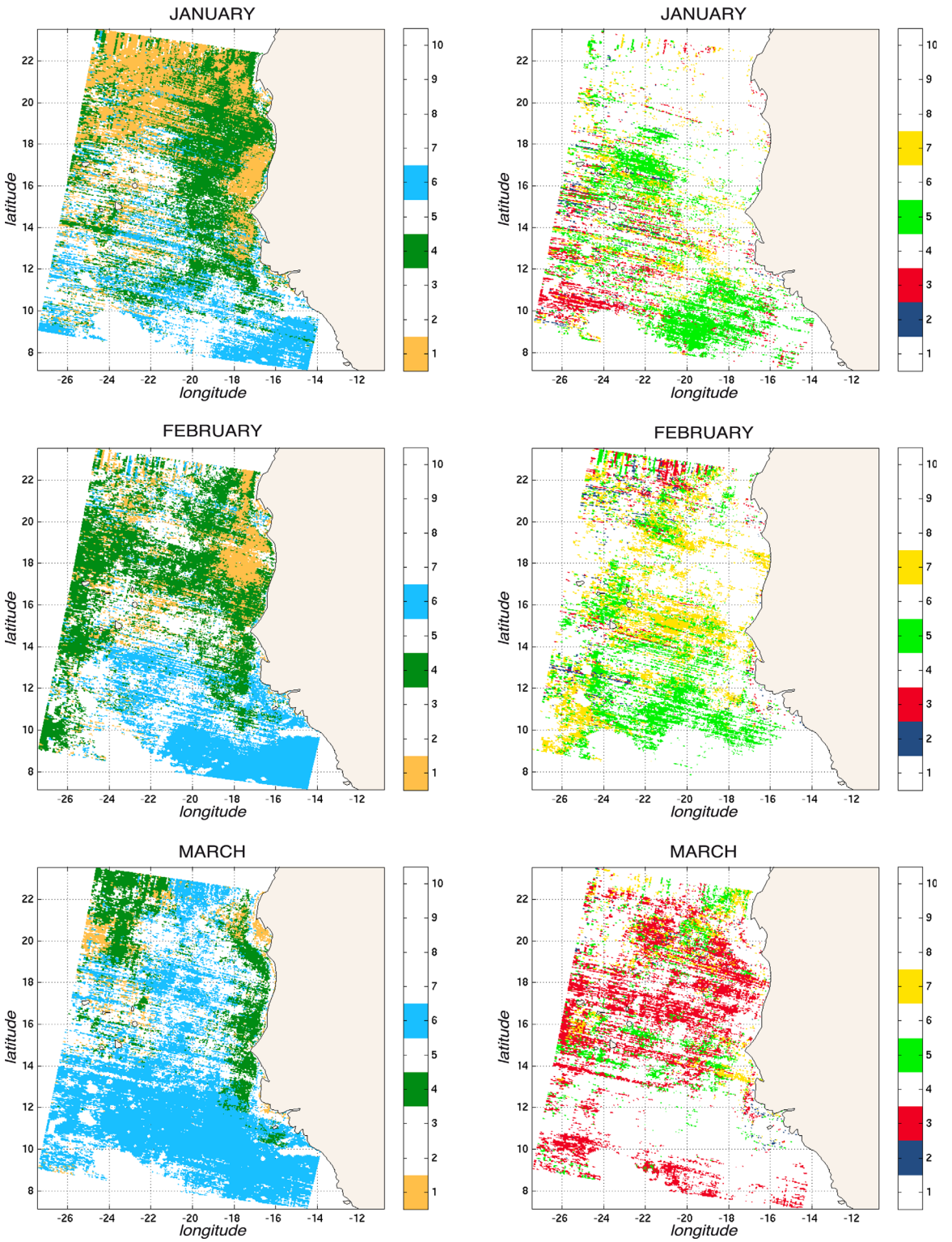

Figure 7b. The 13 year climatology of the classes for January, February, and March. (left) We have represented class-1 (*orange*), class-4 (*green*), and class-6 (*light blue*). (right) We have represented class-2 (*blue*), class-3 (*red*), class-5 (*light green*), and class-7 (*yellow*).

Class-5 is encountered during winter (December, January, February) quite far offshore, mainly in the northern part of the studied region; it disappears in March. Its behavior seems closely related to that of class-4.

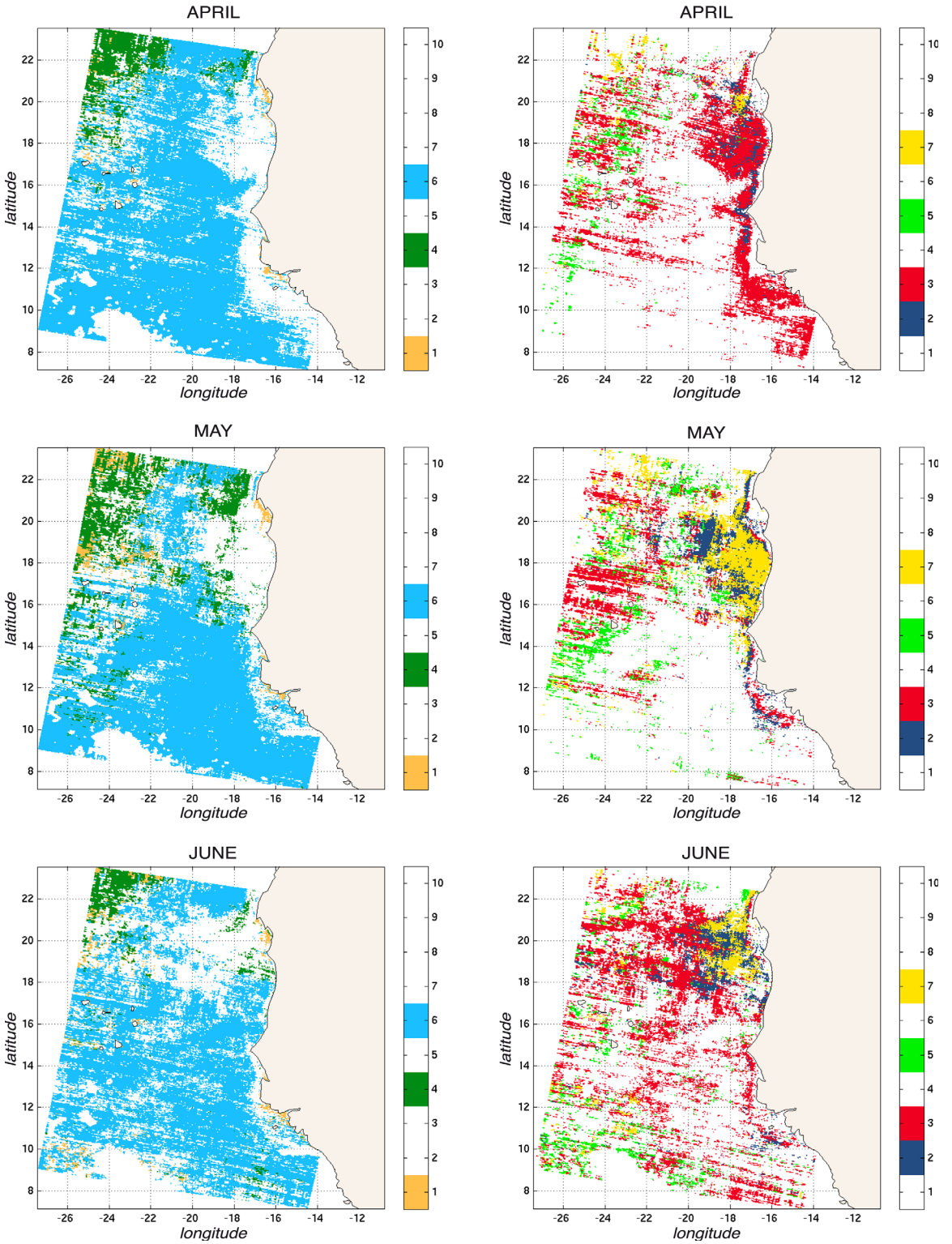

Figure 7c. The 13 year climatology of the classes for April, May, and June. (left) We have represented class-1 (*orange*), class-4 (*green*), and class-6 (*light blue*). (right) We have represented class-2 (*blue*), class-3 (*red*), class-5 (*light green*), and class-7 (*yellow*).

6. Upwelling Scenario and Class Labeling

The well-marked seasonality of the different classes and the stability of their patchiness from one year to another incited us to assign a specific phytoplankton group to each class. The difficulty, when trying to

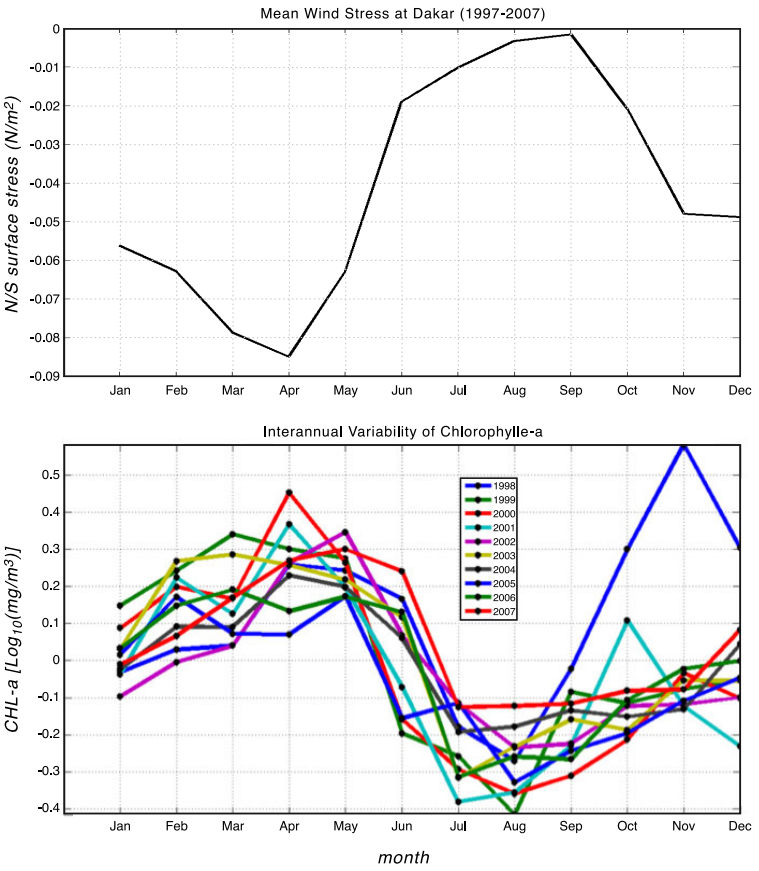

Figure 8. Seasonal variability of the (top) meridional wind stress component at Dakar and (bottom) chlorophyll-*a* concentration averaged over the studied zone for the different years.

attribute such a group to a spectrum class, is that we do not have enough in situ measurements collocated with satellite ocean-color observations permitting a statistically significant labeling of the classes. This is why we decided to tentatively label the classes according to the shape of their spectrum following the labeling given by *Ben Mustapha et al.* [2014], on the one hand, and from their ecological properties, on the other hand; i.e., by studying the location and the seasonal occurrence of the different classes. This is supported by the fact that the spectral shapes of the different classes are well identified, their intraneuron variance is quite small, as seen in Figure 5, and the seasonal and spatial evolution of the patterns of the different classes is well defined. Additionally, these spectra are very little affected by the atmospheric characteristics, as shown in Figure 6.

In order to understand the impact of the upwelling on the classes, we computed the monthly mean meridional wind stress component at Dakar (Figure 8), which is a good estimate of the mean wind stress component parallel to the coast. This mean stress component is responsible for the Senegalo-Mauritanian upwelling by generating an offshore Ekman transport which drives an upward vertical velocity transporting nutrients from the deep layers of the ocean to the surface, and consequently activating the development of phytoplankton [*Farikou et al.*, 2013]. The upwelling starts developing in October when the trade winds begin to blow; its physical intensity (i.e., the vertical velocity) is maximum in April (highest meridional wind stress component), as well as its biological activity (highest chlorophyll-*a* concentration in the coastal zone) (Figure 8). Then, the upwelling intensity (both physical and biological components) begins to weaken when the trade winds decrease. It disappears in July, August, and September, a period corresponding to the African monsoon, and starts increasing again in October.

From the shape of the $Ra(\lambda)$ spectra associated with the classes (Figure 6), the class climatology (Figures 7a–7c), and the seasonal variation of the wind (Figure 8) which triggers the upwelling and determines its intensity, we can outline the following scenario for the phytoplankton groups and consequently tentatively label the groups:

The Senegalo-Mauritanian upwelling begins to develop at the end of October with the onset of the trade winds, which intensify (Figure 8) as the season progresses. In November, we note the development of class-1 waters in the northern part of the region associated with the extent of the Mauritanian upwelling. Class-1 water is predominant in December off the Mauritanian coast, in the northern part of the studied region (Figure 7a) where they extend far offshore, which is a characteristic of the Mauritanian upwelling [*Lathuilière et al*., 2008]. Class-1 water is then encountered along the coast of Senegal in January (down to 12°N) and in February (Figure 7b) where it forms quite large patches which are still present in March and completely disappear in April. Their $Ra(\lambda)$ spectrum is lower than one, meaning that the associated phytoplankton absorbs light more than it scatters it (the associated phytoplanktons do not have a skeleton). Class-1 can be considered as the signature of a phytoplankton bloom associated with haptophytes, later on reported as nanoeukaryotes by *Alvain et al*. [2012]; these tiny algae have a high specific absorption of light and respond to moderate nutrient supply. Abundance of nanoeukaryotes in this region was also noted by *Tarran et al*. [2006] during AMT 13 and AMT 14 cruises, using flow cytometry.

Class-1 water is associated with class-4 water, which can extend quite far offshore west of class-1 water in the northern part of the studied region. Its $Ra(\lambda)$ spectrum is around 1.25 and may correspond to *Prochlorococcus*, which dominate in oligotrophic tropical waters [*Partensky et al*., 1999]. Indeed, this genus is dominant everywhere in the tropical oligotrophic zones of the ocean [*Partensky et al*., 1999]. Class-1 disappears in March while class-4 is still present along the coast. These two classes are completely absent in April.

Class-6 $Ra(\lambda)$ spectra water is abundant in the southern part of the studied region and may correspond to equatorial oligotrophic waters origining in the North Equatorial Counter-Current and the Guinea dome. These waters progress northward from April to November associated with the displacement of the ITCZ [Siedler *et al*., 1992]. Owing to its quite high $Ra(\lambda)$ value (mean around 2), class-6 water may be associated with *Synechococcus*-like Cyanobacteria (SLC) which are abundant in oligotrophic tropical waters, but may benefit from small nutrient enrichment, as reported by *Partensky et al*. [1996].

Class-2 and class-3 waters, which are quasi-absent at the beginning of winter, are quite abundant offshore in March mainly north of 14°N and predominate in the coastal area in April (mainly class-3 waters; Figure 7c) when the upwelling intensity is maximal (Figure 8). They are still present in May (mainly as class-3) along the coast. In April, these two classes are located in coastal regions where the chlorophyll-*a* concentration is high; their $Ra(\lambda)$ spectrum is greater than 1.6, meaning the phytoplankton species constituting these classes have a skeleton reflecting the light; they may correspond to diatoms, which grow very fast when nutrients are abundant, producing blooms, and actively export organic carbon to depth. Class-2 and class-3 are close together on the SOM map (Figure 3) and are associated with two connected dendogram branches (Figure 4). In May, class-2 and class-3 begin to vanish in the coastal area but are still present offshore where they mix with class-6 water. We observe a large patch of class-7 water in the coastal area between 17°N and 20°N replacing class-3 water. Classe-2 and class-3 are still present offshore in June, and are mainly encountered offshore north of 14°N. Then these two classes disappear from the coastal upwelling area until the following March. Diatoms are in fact the group that responds best to upwelling conditions. It might be surprising that diatoms are not seen in December–February when the upwelling intensifies. The statistical method does not say that they are absent during that period but that they are not the most abundant species. This is the major drawback of the classification methodology we used, which is an all-or-nothing method. In fact, the diatoms are seen in March, at the end of the nanoeukaryote bloom, and cover large oceanic surfaces in June at the end of the diatom bloom of April, showing that they are present as a background species in the studied region.

Satellite observations indicate that the biological response to the upwelling appears to be bimodal: we note a first coastal phytoplankton bloom dominated by nanoeukaryotes during the onset of the upwelling (January–February) coming from the Mauritanian waters and progressing southward, which weakens in March. We note a second coastal bloom dominated by diatoms in April-May when the vertical velocities associated with the upwelling are maximum, as shown in Figure 8a, representing the North-South component of the wind stress.

This scenario, which was obtained from satellite observation only, is compatible with the known ecological dynamics of upwelling regions: the nanoeukaryotes and the diatoms being the dominant species in the

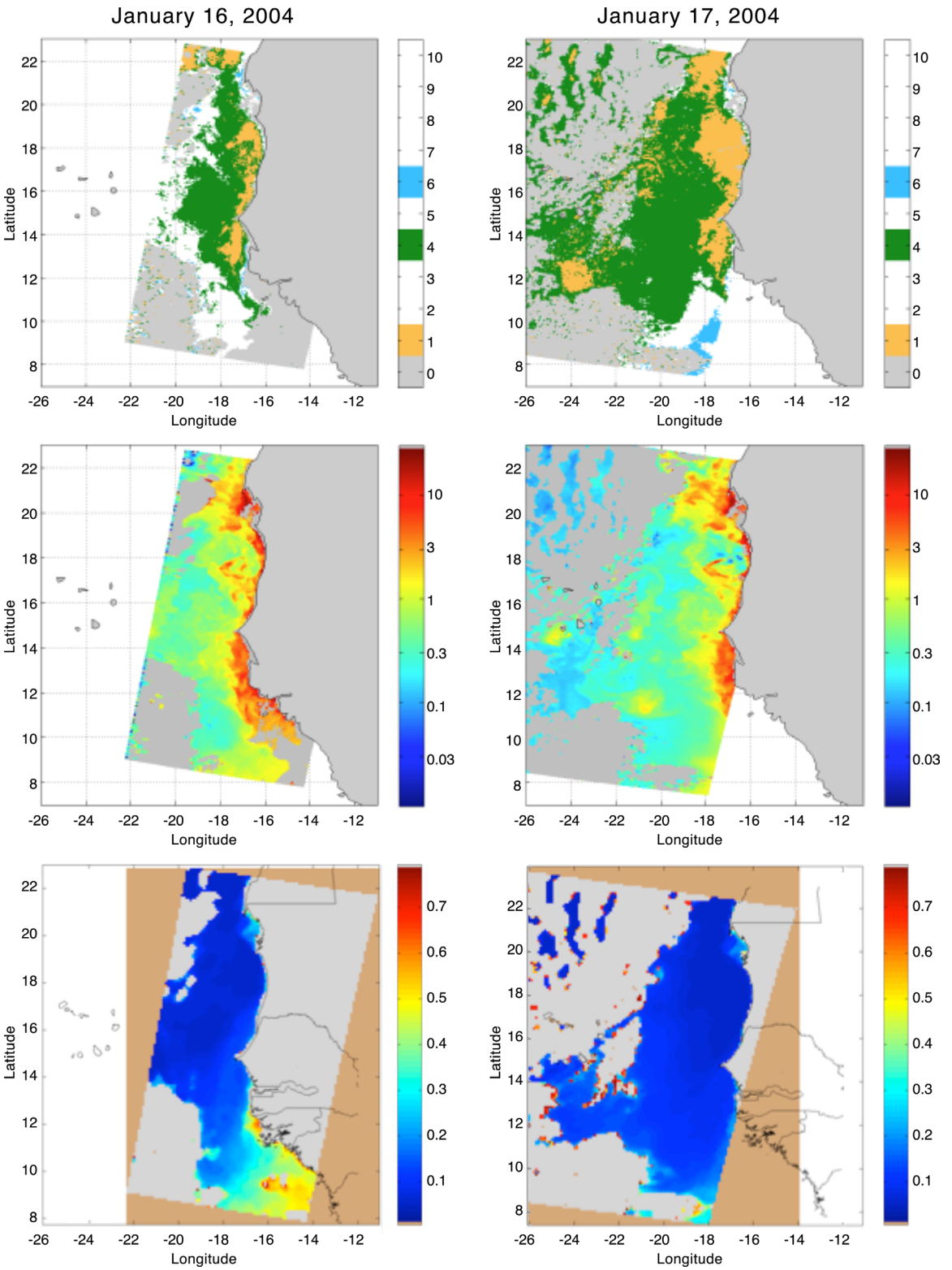

Figure 9a. (top) Spectrum pattern of class-1, class-4, and class-6, (middle) the associated chlorophyll-*a* concentration, and (bottom) AOT for the 16 and 17 January 2004, days for which AOT coverage was very low. Class-1 (haptophytes) is in *orange*, class-4 (*Prochlorococcus*) in *green*, and class-6 (SLC) in *light blue*. AOT low values are in *blue*.

coastal upwelling area, the diatoms predominating when the chlorophyll-*a* concentration is maximum; i.e., when the nutrient concentration is maximum. The replacement of these phytoplankton groups by "SLC" (class-6) when the upwelling stops, is also in agreement with current knowledge of the biological

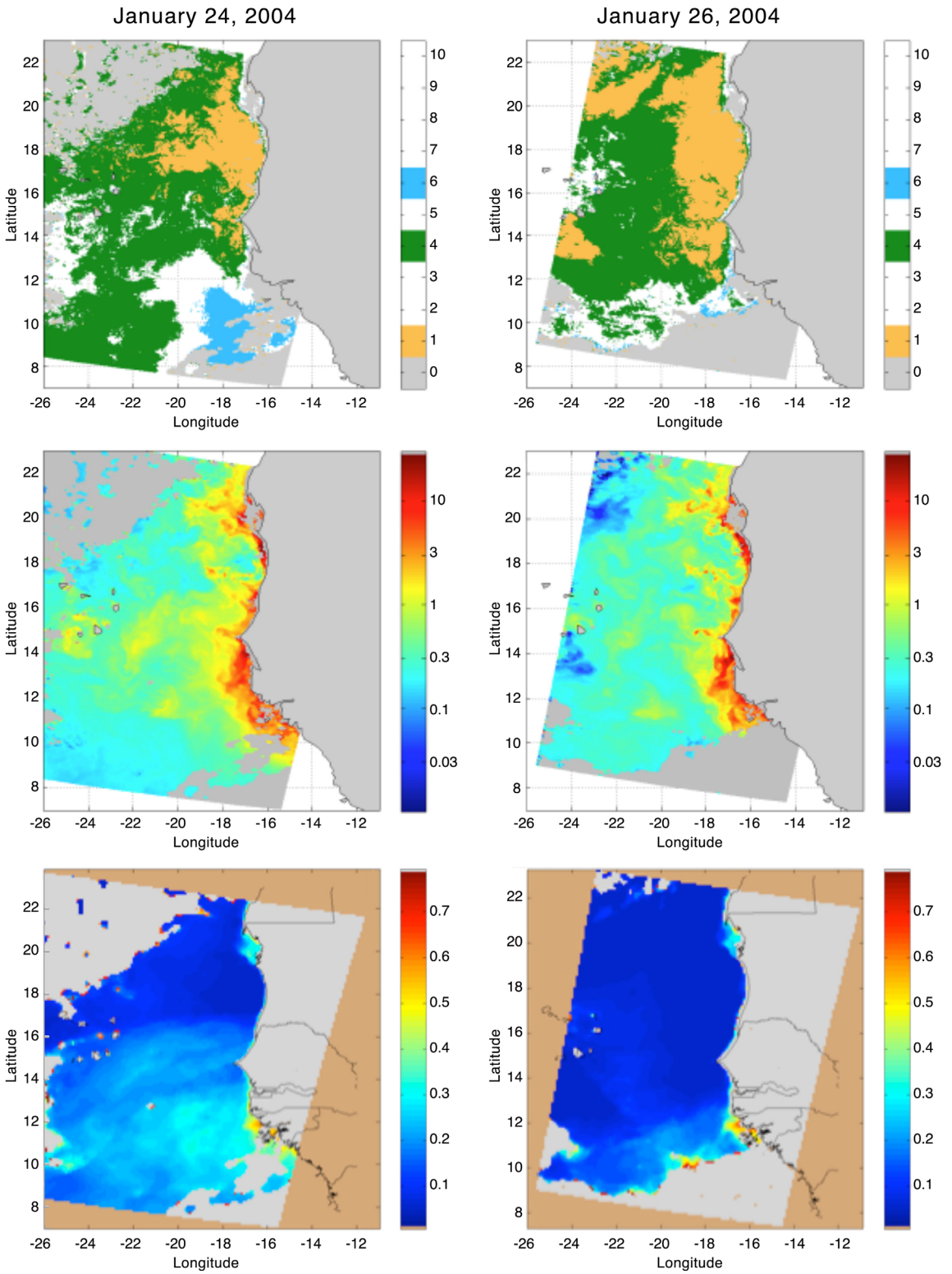

Figure 9b. (top) Spectrum pattern of class-1, class-4, and class-6, (middle) the associated chlorophyll-*a* concentration, and (bottom) AOT for the 24 and 26 January 2004, days for which AOT coverage was very low. Class-1 (haptophytes) is in *orange*, class-4 (*Prochlorococcus*) in *green*, and class-6 (SLC) in *light blue*. AOT low values are in *blue*.

functioning of the North Atlantic Canary upwelling from in situ observations [*Gibb et al.*, 2000; *Aiken et al.*, 2009; *Hirata et al.*, 2011]. Predominance of "*Prochlorococcus*" (class-4) immediately after the first upwelling bloom in January–February is less convincing, as this cyanobacterium is known to be specific to poor

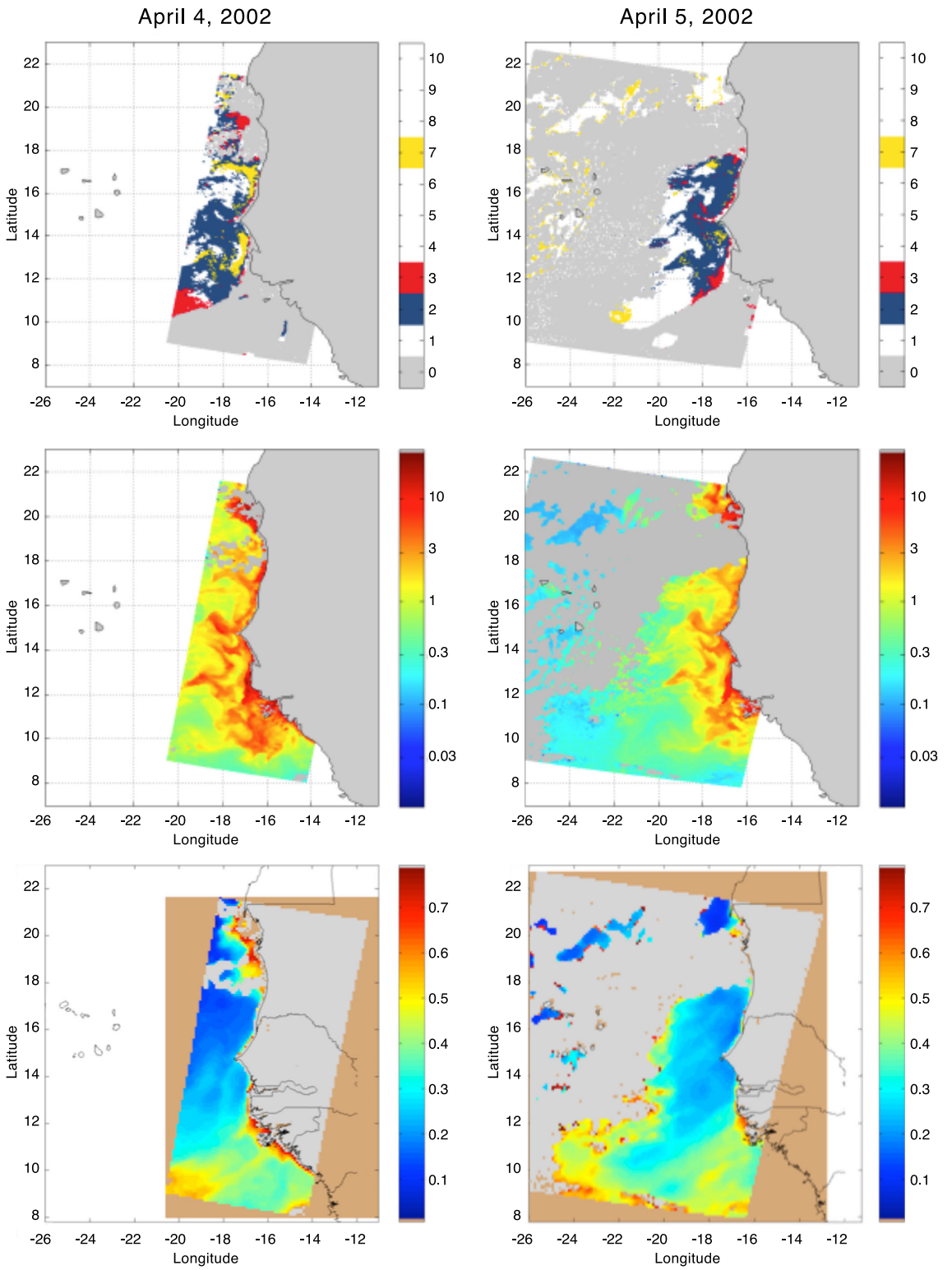

Figure 10. (top) Spectrum pattern of class-2, class-3, and class-7, (middle) the associated chlorophyll-a concentration, and (bottom) AOT for 4 and 5 April, days for which AOT coverage was low in the regions where we computed the classes. Class-2 and class-3 (diatoms) are in *blue* and *red*, class-7 in *yellow*. AOT low values are in *blue*.

tropical waters, where it is often associated with SLC. Besides, class-4 "*Prochlorococcus*" spectra, which are characterized by low values, may be caused by nanoeukaryotes in the upper range of their usual spectral properties.

We were unable to label class-5 and class-7, which may be associated with a mixing of different groups.

In order to better understand this description, we isolated two sequences of several days, one dedicated to class-1 bloom (a "nanoeukaryote" bloom), the other to class-2 and class-3 blooms ("diatom" bloom), for which we can follow the development of the pattern of the two classes.

We selected a 4 day period in January 2004 (16, 17, 24, and 26), which was characterized by the "nanoeukaryote" bloom (Figures 9a and 9b) for which the AOT is small. The chlorophyll-*a* concentration images (Figures 9a and 9b, middle) show a well-developed upwelling with a very high chlorophyll-*a* concentration at the coast. The mean chlorophyll-*a* concentration decreases offshore. Chlorophyll-*a* is advected offshore by filaments, which can persist for several days; see as an example the "hook-like meanders" off Cap Vert at Dakar (15°N) and off the mouth of the Senegal River (16°N) in the 24 January image. We note very high chlorophyll-*a* concentrations over the Arguin Bank (20°N) and south of Cap Vert on the Siné-Saloum Shelf (14°N), the Guinea Bank (13°N–11°N). The spectral signature maps (Figures 9a and 9b, top) show that class-1 water is located near the coast (in a region extending several tens of kilometers offshore) forming a strip parallel to the coast; this strip is surrounded by class-4 water ("*Prochlorococcus*"), which can extend quite far to the west and is sometimes encountered near the coast replacing class-1 water. The interpretation of this image sequence is in agreement with the upwelling scenario described above. The variation in the extent of class-1 between 16 and 17 January and between 24 and 25 January is due to the clustering method; small variations in a group concentration may change its class assignment, depending on its concentration rating, and consequently modifying its geographical distribution. There is no correlation between AOT (Figures 9a and 9b, bottom) and the classes. We also selected a 2 day period, 4 and 5 April 2002, for which the diatoms are predominant according to the previous climatology. Class-2 and class-3 waters (Figure 10) indicate the presence of "diatoms" in the coastal upwelling area. These classes replace class-1 ("nanoeukaryotes") observed in January and February in the coastal area, which has completely disappeared. These daily images confirm the analyses done on the monthly climatology. As for the January images, there is no correlation between AOT (Figure 10, bottom) and the classes.

Our labeling, which is based on the results of *Ben Mustapha et al*. [2014], on the one hand, and on historical in situ measurements, on the other hand [*Blasco et al*., 1980; *Dia*, 1985], is given with a high probability due to the 13 years of satellite observations. It leads to a coherent seasonal scenario for the phytoplankton groups in agreement with the upwelling dynamics. But the labeling may fail in some situations due to the specificity of the studied region.

7. Discussion and Conclusion

Our neural classification procedure has led us to identify 10 classes of reflectance ratio spectra, $Ra(\lambda)$, defined as the water-leaving radiance spectrum, $\rho_w(\lambda)$, normalized by a $\rho_W^{ref}(\lambda$, Chl-*a*) spectrum, which is a simple model of $\rho_W(\lambda)$ depending on the SeaWiFS standard chlorophyll-*a*. The 10 classes are well characterized, most of them presenting a well-defined pattern with a small intraneuron dispersion (Figure 4). Their patchiness is very coherent both in space and time, but their labeling is very challenging. A first analysis permitted us to reject three classes (class-8, class-9, and class-10) of our study as corresponding to case-2 waters situated at very shallow coastal locations (Arguin Bank, shelves off the coast of Casamance and Guinea; see Figure 1). The interpretation of these waters is beyond the scope of the present paper, as argued in section 4. We therefore only analyzed the remaining seven classes. This is in agreement with *Farikou et al*. [2013] who also noted the presence of waters whose ocean-color spectra correspond to case-2 waters at these coastal locations.

By generating a monthly climatology of $Ra(\lambda)$ associated with AOT < 0.35 for 13 years of observation and after inspecting a large number of situations for which AOT is small, we were able to outline a scenario for interpreting the spatial variability of the spectra in terms of phytoplankton groups in the Senegalo-Mauritanian upwelling region. In this scenario we identified some $Ra(\lambda)$ spectral classes to phytoplankton groups according to the labeling given by *Ben Mustapha et al*. [2014], on the one hand, and on the coherent

geographical position and seasonal evolution of the pattern of the different classes, on the other hand. The major feature of the Senegal upwelling is the bimodality of the phytoplankton bloom. We observe a first bloom dominated by class-1 (labeled as "nanoeukaryote" type) occurring during a quite long period corresponding to the onset of the upwelling (December to mid-March). This class predominates in the Mauritanian waters (north of 21°N) in December (Figure 7a) and progresses southward until mid-March (Figure 7b) reaching 12°N. It is accompanied by class-4 ("*Prochlorococcus*" type) water, which is mainly encountered offshore in January and replaces class-1 in March. We noted a second bloom close to the coast and much shorter in April, May, when the chlorophyll-*a* concentration is maximum. It is dominated by class-2 and class-3 (labeled as "diatom" type). In March, the coastal bloom of class-1 ("nanoeukaryote") has vanished and we note a northward progression of class-6 water (SLC type), which dominates in the southern part of the region and corresponds to equatorial oligotrophic water originating in the NECC and the Guinea dome. This water moves northward from April to November associated with the ITCZ displacement. The diatoms, which present a maximal coastal bloom in April, seem to be present as a background type mixed with SLC type (class-6 water) from March to June north of 14°N.

This well-marked seasonal variability of the different classes is in agreement with in situ observations of phytoplankton reported in *Blasco et al*. [1980] in March to May 1974 in this region during the JOINT I experiment. These authors analyzed 740 water samples collected with Niskin bottles at 136 stations extending along a line at 21°40′N (in the northern part of our study region) from 0 to 100 km offshore. The samples were taken at several depths (mostly at 5, 15, 30, 50, and 100 m). Phytoplankton cells were counted and identified by the Utermohl inverted microscope technique [*Blasco*, 1977]. They found that diatoms reach their maximum concentration in April–May and are the most abundant group in that period, while the other cells predominate in March. It is also interesting to notice that these other cells were generally situated in the upper 30–40 m layer, making their detection by satellite ocean-color radiometry easier than for the diatoms which have a deeper distribution. This reinforces the fact that we observed a dominance of class-1 (nanoeukaryotes) from December to March, even if diatoms are abundant in that period. Similar microscope observations have been reported in the ocean area south of Dakar by *Dia* [1985] during several ship surveys in February–March 1982–1983. This latter study also mentioned the bimodality of the phytoplankton bloom of the Senegal-Mauritanian upwelling system.

Our scenario is also in agreement with the phytoplankton types determined by measuring photosynthetic pigments using high-performance liquid chromatography (HPLC) during two series of cruises in the region: the EUMELI cruises in September–October 1991 and in May–June 1992 [*Claustre and Marty*, 1995], and the Atlantic Meridional Transect (AMT) starting in 1995 up to 2005 [*Robinson et al*., 2006]. Observations made during these cruises showed that the picoplankton (less than 2 μm) generally predominates [*Partensky et al*., 1999; *Gibb et al*., 2000; *Tarran et al*., 2006; *Aiken et al*., 2009] and found as a background in our satellite observations (class-4). *Partensky et al*. [1996] also noted the large abundance of *Synechococcus* at the EUMELI mesotrophic station in the plume of the Mauritanian upwelling in June 1992. Diatoms, however, often make up most of the biomass in the upwelling zone close to the coast of Mauritania, as indicated by the relative abundance of the fucoxanthin pigment mainly at the end of the upwelling season [*Aiken et al*., 2009] as in our satellite observations.

Our analysis agrees with the original PHYSAT method reported in the recent works of *Alvain et al*. [2012] and *Ben Mustapha et al*. [2014]. In the latter paper, we clearly see the predominance of nanoeukaryotes in January (their Figure 11, top) and the presence of some diatoms in June (their Figure 12, top) off the coast of Sénégal. The major advantages of our processing with respect to that of *Alvain et al*. [2005, 2012] and *Ben Mustapha et al*. [2014] is to use a more efficient atmospheric correction (SOM-NV), as described by *Diouf et al*. [2013], than the one used in the standard SeaWiFS processing. SOM-NV is expected to give ocean spectra of better quality, and consequently to increase the number of valid pixels by an order of magnitude.

The atmosphere does not seem to affect the spectrum shape dramatically, as shown in Figure 6 (except for class-8, class-9, and class-10 associated with coastal waters, which could be strongly influenced by coastal aerosols), nor the class patterns (Figures 9a, 9b, and 10). A class of reflectance spectrum ratio can be considered as a qualitative index of the presence (but not of the absence) of a specific phytoplankton group. In fact, the passage from one class to another, which is an all-or-nothing process, does not take into account the smooth variations in the natural environment, especially in the vicinity of a class boundary, where several phytoplankton groups can coexist together in the same area at different concentrations.

The geographical pattern and seasonal behavior of the classes associated with their statistical properties (dendogram and topology of SOM) led us to envisage merging some classes. Class-2 and class-3 ("diatom" type) and class-7 and class-6 whose spectral shapes are similar and which are associated with two dendogram branches both connected to the same branch, might be merged, although each class has its own ecological dynamics, as shown by the monthly climatology. The merging of class-2 and class-3 is feasible, but the replacement of class-3 ("diatom" type) by class-7 water (and consequently by class-6 water if class-7 and class-6 were merged) in May, as shown in Figure 7c, is difficult to justify.

A major advantage of our method is to use daily satellite observations to construct the monthly climatology of the classes for 13 years (1998–2010) of the SeaWiFS observations. Due to the highly nonlinear character of the algorithms for determining the classes, it is more rigorous mathematically to apply these algorithms to daily data and to average the daily estimate of the classes for each month as described in section 5 than to estimate the classes from monthly satellite data as many authors did [*Uitz et al*., 2010; *Hirata et al*., 2011].

The PHYSAT method combined with an efficient clustering method like SOM and an advanced atmospheric correction algorithm such as SOM-NV [*Diouf et al*., 2013] constitutes a powerful tool for extracting biological information from satellite ocean-color observations at global scale [*Ben Mustapha et al*., 2014] as well as at a regional scale, as in the present study. As in its latter version PHYSAT has been calibrated on 1068 coincident in situ and satellite measurements [*Ben Mustapha et al*., 2014], it can be used with some confidence to explore regions where no in situ observations have been made. The method is easy to handle and could be used to quickly extract qualitative information on newly studied areas. But, as with many clustering methods, PHYSAT presents intrinsic limitations. It is an all-or-nothing method, giving only the predominant group. Representation of an area where several groups coexist with a close reflectance ratio poses a problem. To mitigate this drawback, it would be necessary to develop a clustering method giving the probabilities of the different elements to belong to a given class. Moreover, it would be interesting to combine PHYSAT and recent methods developed for retrieving phytoplankton groups dealing with chlorophyll-*a* concentration, such as those described by *Devred et al*. [2006] and *Uitz et al*. [2006, 2010] and revisited by *Mouw and Yoder* [2010] and *Hirata et al*. [2011], which would offer the advantage of increasing the information content of the phytoplankton retrieval methodology.

Our processing could be improved by combining many field data such as cell size, dissolved colored organic matter, phytoplankton absorption spectra, and of sea surface phenomena, such as wind intensity, since we process second-order effects cleared of chlorophyll-*a* concentration.

In addition to the present PHYSAT processing, which considers only reflectance spectrum ratios that decrease or increase regularly from 410 to 555 nm, we could also consider reflectance spectrum ratios with peaks or troughs, which appear frequently in ocean-color data. Interpretation of such spectra however remains difficult and will necessitate adequate methodological developments.

Our paper aimed to analyze a very active oceanic region in biological terms with strong economic impacts on fisheries in Senegal and Mauritania. Since this region has been poorly surveyed in situ, we have chosen to extract pertinent scientific information from the satellite measurements. Satellite sensors provide a tremendous amount of data, which have remained unexploited due to the lack of scientists and of adequate methods for processing large data sets. This satellite information should help to improve the understanding of the functioning of this very productive region, to detect the points of interest such as the two phytoplankton blooms observed in the satellite data which are quite surprising and ultimately contribute to defining new lines of research. It should also help to improve the design of oceanographic cruises and the optimization of the research vessel tracks for in situ sampling purposes.

Acknowledgments
The study was supported by the project CNES-TOSCA 2011-2012. The water-leaving reflectances were obtained from the SeaWiFS daily reflectances, $\rho^{obs}_{TOA}w(\lambda)$, provided by the NASA/GSFC/DAAC observed at the top of the atmosphere (TOA) and processed with the SOM-NV algorithm [*Diouf et al*., 2013] from 1998 to 2010. They are available at the web site: http://poacc.locean-ipsl.upmc.fr/. We thank Ray Griffiths for editing the manuscript.

References

Aiken, J., Y. Pradhan, R. Barlow, S. Lavender, A. Poulton, P. Holligan, and N. J. Hardman-Mountford (2009), Phytoplankton pigments and functional types in the Atlantic Ocean: A decadal assessment, 1995-2005, *Deep Sea Res., Part II*, *56*, 889–917.

Alvain, S., C. Moulin, Y. Dandonneau, and F. M. Breon (2005), Remote sensing of phytoplankton groups in case-1 waters from global SeaWiFS imagery, *Deep Sea Res., Part I*, *52*(11), 1989–2004.

Alvain, S., H. Loisel, and D. Dessailly (2012), Theoretical analysis of ocean color radiances anomalies and implications for phytoplankton group detection, *Opt. Express*, *20*(2), 1070–1083.

Antoine, D., J. M. André, and A. Morel (1996), Oceanic primary production: 2. Estimation at global scale from satellite (coastal zone color scanner) chlorophyll, *Global Biogeochem. Cycles*, *10*(1), 57–69, doi:10.1029/95GB02832.

Badran, F., M. Yacoub, and S. Thiria (2005), Self-organizing maps and unsupervised classification, in *Neural Networks, Methodology and Applications*, edited by G. Dreyfus, chap. 7, pp. 379–442, Springer, Berlin.

Behrenfeld, M. J., and P. G. Falkowski (1997), Photosynthetic rates derived from satellite-based chlorophyll concentration, *Limnol. Oceanogr.*, *42*, 1–20.

Behrenfeld, M. J., R. T. O'Malley, D. A. Siegel, C. R. McClain, J. L. Sarmiento, G. C. Feldman, A. J. Milligan, P. G. Falkowski, R. M. Letelier, and E. S. Boss (2006), Climate-driven trends in contemporary ocean productivity, *Nature*, *444*, 752–755, doi:10.1038/nature05317.

Ben Mustapha, Z., S. Alvain, C. Jamet, H. Loisel, and D. Desailly (2014), Automatic water leaving radiance anomalies from global SeaWiFS imagery: Application to the detection of phytoplankton groups in open waters, *Remote Sens. Environ.*, *146*, 97–112.

Bishop, C. (2006), *Pattern Recognition and Machine Learning*, Springer, Berlin.

Blasco, D. (1977), Red tide in the upwelling region of Baja California, *Limnol. Oceanogr.*, *22*, 255–263.

Blasco, D., M. Estrada, and B. Jones (1980), Relationship between the phytoplankton distribution and composition and the hydrography in the northwest African upwelling region, near Cabo Corbeiro, *Deep Sea Res., Part A*, *27*, 799–821.

Ciotti, A., and A. Bricaud (2006), Retrievals of a size parameter for phytoplankton and spectral light absorption by colored detrital matter from water-leaving radiances at SeaWiFS channels in a continental shelf region off Brazil, *Limnol. Oceangr. Methods*, *4*, 237–253.

Claustre, H., and J. C. Marty (1995), Specific phytoplankton biomasses and their relation to primary production in the tropical North Atlantic, *Deep Sea Res., Part I*, *42*(8), 1475–1493, doi:10.1016/0967-0637(95)00053-9.

Demarcq, H., and V. Faure (2000), Coastal upwelling and associated retention indices from satellite SST. Application to *Octopus vulgaris* recruitment, *Oceanogr. Acta*, *23*, 391–407.

Devred, E., S. Sathyendranath, V. Stuart, H. Maas, O. Ulloa, and T. Platt (2006), A two component model of phytoplankton absorption in the open ocean: Theory and applications, *J. Geophys. Res.*, *111*, C03011, doi:10.1029/2005JC002880.

Dia, A. (1985), Biomasse et biologie du phytoplancton le long de la petite côte sénégalaise et relations avec l'hydrologie, intern. report, n°44, CRODT (DAKAR). [Available at http://www.sist.sn/gsdl/collect/publi/index/assoc/HASH2127.dir/doc.pdf.]

Diouf, D., A. Niang, J. Brajard, M. Crepon, and S. Thiria (2013), Retrieving aerosol characteristics and sea-surface chlorophyll from satellite ocean color multi-spectral sensors using a neural-variational method, *Remote Sens. Environ.*, *130*, 74–86.

Farikou, O., S. Sawadogo, A. Niang, J. Brajard, C. Mejia, M. Crépon, and S. Thiria (2013), Multivariate analysis of the Senegalo-Mauritanian area by merging satellite remote sensing ocean color and SST observations, *J. Environ. Earth Sci.*, *5*(12), 756–768.

Gibb, S. W., R. G. Barlow, D. G. Cummings, N. W. Rees, C. C. Trees, P. Holligan, and D. Suggett (2000), Surface phytoplankton pigment distributions in the Atlantic Ocean: An assessment of basin scale variability between 50°N and 50°S, *Progr. Oceanogr.*, *45*, 339–368.

Hirata, T., J. Aiken, N. Hardman-Mountford, T. J. Smyth, and R. G. Barlow (2008), An absorption model to determine phytoplankton size classes from satellite ocean color, *Remote Sens. Environ.*, *112*, 3153–3159.

Hirata, T., et al. (2011), Synoptic relationships between surface chlorophyll-*a* and diagnostic pigments specific to phytoplankton functional types, *Biogeosciences*, *8*(2), 311–327.

Jain, A. K., and R. C. Dubes (1998), *Algorithms for Clustering Data, Prentice Hall Adv. Ref. Ser.*, 320 pp., Prentice Hall, Englewood Cliffs, N. J.

Jouini, M., M. Lévy, M. Crépon, and S. Thiria (2013), Reconstruction of ocean color images under clouds using a neuronal classification method, *Remote Sens. Environ.*, *131*, 232–246.

Kohonen, T. (1982), Self-organized formation of topologically correct feature maps, *Biol. Cybern.*, *43*, 59–69.

Kohonen, T. (2001), *Self-Organizing Maps*, 3rd ed., Springer, Berlin.

Lachkar, Z., and N. Gruber (2012), A comparative study of biological production in eastern boundary upwelling systems using an artificial neural network, *Biogeosciences*, *9*, 293–308.

Lathuilière, C., V. Echevin, and M. Levy (2008), Seasonal and intraseasonal surface chlorophyll-*a* variability along the northwest African coast, *J. Geophys. Res.*, *113*, C05007, doi:10.1029/2007JC004433.

Longhurst, A., S. Sathyendranath, T. Platt, and C. Caverhill (1995), An estimate of global primary production in the ocean from satellite radiometer data, *J. Plankton Res.*, *17*, 1245–1271.

Morel, A. (1980), In-water and remote measurement of ocean color, *Boundary Layer Meteorol.*, *18*, 177–201.

Mouw, C. B., and J. A. Yoder (2010), Optical determination of phytoplankton size composition from global SeaWiFS imagery, *J. Geophys. Res.*, *115*, C12018, doi:10.1029/2010JC006337.

Niang, A., F. Badran, C. Moulin, M. Crépon, and S. Thiria (2006), Retrieval of aerosol type and optical thickness over the Mediterranean from SeaWiFS images using an automatic neural classification method, *Remote Sens. Environ.*, *100*, 82–94.

O'Reilly, J. E., S. Maritorena, B. G. Mitchell, D. A. Siegel, K. L. Carder, S. A. Garver, M. Kahru, and C. McClain (1998), Ocean color chlorophyll algorithm for SeaWiFS, *J. Geophys. Res.*, *103*(C11), 24937–24953.

Partensky, F., J. Blanchot, F. Lantoine, J. Neveux, and D. Marie (1996), Vertical structure of picophytoplankton at different trophic sites of the tropical northeastern Atlantic Ocean, *Deep Sea Res.*, Part 1, *43*(8), 1191–1213.

Partensky, F., J. Blanchot, and D. Vaulot (1999), Differential distribution and ecology of *Prochlorococcus* and *Synechococcus* in oceanic waters: A review, *Bull. Inst. Océanogr.*, *19*, 457–475.

Prieur, L., and S. Sathyendranath (1981), An optical classification of coastal and oceanic waters based on the specific spectral absorption of phytoplankton pigments, dissolved organic matter and other particulate materials, *Limnol. Oceanogr.*, *26*, 671–689.

Robinson, C., et al. (2006), The Atlantic Meridional Transect (AMT) programme: A contextual view 1995-2005, *Deep Sea Res., Part II*, *53*(14-16), 1485–1515.

Sathyendranath, S., L. Watts, E. Devred, T. Platt, C. M. Caverhill, and H. Maass (2004), Discrimination of diatom from other phytoplankton using ocean-colour data, *Mar. Ecol. Prog. Ser.*, *272*, 59–68, doi:10.3354/meps272059.

Sawadogo, S., J. Brajard, A. Niang, C. Lathuilière, M. Crepon, and S. Thiria (2009), Analysis of the Senegalo-Mauritanian upwelling by processing satellite remote sensing observations with topological maps, in *Proceedings IEEE International Joint Conference on Neural Networks*, *IJCNN*, pp. 2826–2832, Atlanta, USA.

Siedler, G., N. Zangenberg, R. Onken, and A. Morlière (1992), Seasonal changes in the tropical Atlantic circulation: Observation and simulation of the Guinea Dome, *J. Geophys. Res.*, *97*(C1), 703–715.

Tarran, G. A., J. L. Heywood, and M. V. Zubkov (2006), Latitudinal changes in the standing stocks of nano- and picoeukaryotic phytoplankton in the Atlantic Ocean, *Deep Sea Res., Part II*, *53*, 1516–1529.

Thiria, S., C. Mejia, F. Badran, and M. Crépon (1993), A neural network approach for modeling nonlinear transfer functions: Application for wind retrieval from spaceborne scaterrometer data, *J. Geophys. Res.*, *98*(C12), 22,827-22,841.

Uitz, J., H. Claustre, A. Morel, and S. B. Hooker (2006), Vertical distribution of phytoplankton communities in open ocean: An assessment based on surface chlorophyll, *J. Geophys. Res.*, *111*, C08005, doi:10.1029/2005JC003207.

Uitz, J., H. Claustre, B. Gentili, and D. Stramski (2010), Phytoplankton class-specific primary production in the world's ocean: Seasonal and interannual variability from satellite observations, *Global Biogeochem. Cycles*, *24*, GB3016, doi:10.1029/2009GB003680.

Westberry, T., M. J. Behrenfeld, D. A. Siegel, and E. Boss (2008), Carbonbased primary productivity modeling with vertically resolved photoacclimation, *Global Biogeochem. Cycles*, *22*, GB2024, doi:10.1029/2007GB003078.